# Indium Phosphide Photonic Integrated Circuits for Coherent Optical Links

Pietro R. A. Binetti, Mingzhi Lu, Erik J. Norberg, Robert S. Guzzon, John S. Parker, Abirami Sivananthan, Ashish Bhardwaj, Leif A. Johansson, *Member, IEEE*, Mark J. Rodwell, *Fellow, IEEE*, and Larry A. Coldren, *Fellow, IEEE*

(*Invited Paper*)

***Abstract*— We demonstrate photonic circuits monolithically integrated on an InP-based platform for use in coherent communication links. We describe a technology platform that allows for the integration of numerous circuit elements. We show examples of an integrated transmitter which offers an on-chip wavelength-division-multiplexing source with a flat gain profile across a 2 THz band and a new device design to provide a flatted gain over a 5 THz band. We show coherent receivers incorporating an integrated widely tunable local oscillator as well as an optical PLL. Finally, we demonstrate a tunable optical bandpass filter for use in analog coherent radio frequency links with a measured spurious-free dynamic range of 86.3 dB-Hz$^{2/3}$ as well as an improved design to exceed 117 dB-Hz$^{2/3}$.**

***Index Terms*— Coherent detection, microwave photonics, monolithic integrated circuits, optical filters, optical receivers, optical transmitters, photonic integrated circuits.**

## I. Introduction

TRADITIONALLY, sufficient performance has been provided by optical links using on-off keying (OOK) for modulating data and direct detection for receiving data. Examples include intensity modulation for digital or analog optical links and time-domain reflectivity for ranging or sensing applications such as pulsed light detection and ranging (LIDAR) or optical time domain reflectometry (OTDR) [1]. Phase encoded signals and the coherent receiver necessary to detect them, such as homodyne detection or heterodyne detection via a local oscillator (LO), are more technically difficult and have been used only where the significant performance or architectural advantages of such links are required. However, in the past decade, interest in coherent optical links has grown for both analog and digital communications because of their increasingly stringent performance requirements.

Today's data traffic in residential, business, and mobile digital communications is mainly driven by a combination of video, social networking and advanced collaboration applications, often referred to as "visual networking." This is illustrated in Figure 1, which shows the current and forecast trend of the Internet data traffic in Exabytes (1 Exabyte = 1E18 Bytes) for some of the most resource-hungry applications, video being the largest [2]. In order to meet the exponentially growing bandwidth demands of such applications, fiber-optic networks need to dramatically increase their capacity to offer a suitable communication infrastructure. This can be done by deploying more fiber channels in parallel, or in a more cost-effective and energy-efficient way, by increasing the spectral efficiency of the existing channels. Thus, enhanced spectral-efficiency (SE) motivated the research and development of more complex modulation formats, such as phase-shift keying (PSK) modulation formats, at the expense of more complex hardware requirements, with respect to the simpler OOK technology [3], [4]. Higher spectral efficiency (SE) is available using quadrature phase-shift keying (QPSK)—double the SE, or polarization-multiplexed QPSK (PM-QPSK) modulation—quadruple the SE, as shown in [5]. A higher sensitivity and improved dispersion compensation is also possible when a coherent optical link is used to (de)modulate real and imaginary parts of the optical signal [3], [5]. Even higher spectral efficiency is possible by modulating both the amplitude and phase, quadature-amplitude modulation (QAM), to more completely utilize the available complex vector-field space, given the signal-to-noise and dynamic range at the receiver, as exhaustively discussed and demonstrated in [5].

Analog optical communications benefit from coherent links as well. Optical phase modulation offers highly-linear optical modulators and very large optical modulation depth, allowing high-dynamic-range optical links to be demonstrated [6]. These benefits extend to sensing as well, where frequency modulated continuous-wave (FMCW) light ranging offers improved sensitivity and resolution compared to time-domain ranging techniques [7].

The larger hardware complexity and cost required for the implementation of a coherent optical link provides motivation for the research and the applications of photonic integrated

Manuscript received August 5, 2011; revised November 3, 2011; accepted November 25, 2011. Date of current version January 24, 2012. This work was supported in part by the Defense Advanced Research Projects Agency Microsystems Technology Office, under Contract including Photonic Integration for Coherent Optics and Photonic Analog Signal Processing Engines with Reconfigurability. Device fabrication was done in the UCSB nanofabrication facility.

P. R. A. Binetti, M. Lu, E. J. Norberg, R. S. Guzzon, J. S. Parker, A. Sivananthan, L. A. Johansson, M. J. Rodwell, and L. A. Coldren, are with the Department of Electrical Engineering, University of California, Santa Barbara, CA 93106 USA (e-mail: pbinetti@ece.ucsb.edu; mlu@ece.ucsb.edu; norberg@ece.ucsb.edu; guzzon@ece.ucsb.edu; JParker@ece.ucsb.edu; asivananthan@umail.ucsb.edu; leif@ece.ucsb.edu; rodwell@ece.ucsb.edu; coldren@ece.ucsb.edu).

A. Bhardwaj was with the Department of Electrical Engineering, University of California, Santa Barbara, CA 93106 USA. He is now with JDS Uniphase Corporation, San Jose, CA 95134 USA (e-mail: Ashish.Bhardwaj@jdsu.com).

Color versions of one or more of the figures in this paper are available online at http://ieeexplore.ieee.org.

Digital Object Identifier 10.1109/JQE.2011.2178590

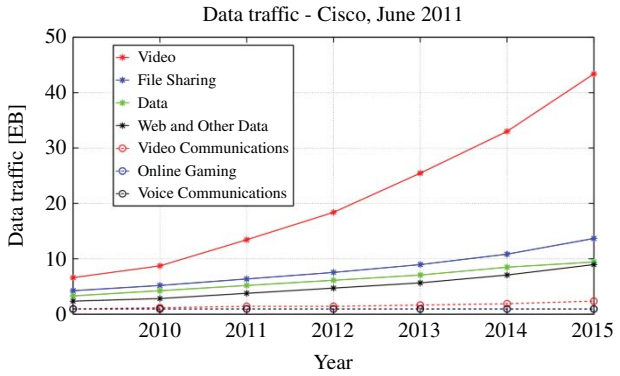


Fig. 1. Cisco "Visual Network Index": current view and forecast of the Internet data traffic (in Exabytes) for some of the most popular applications. Source publicly available at http://www.cicso.com.

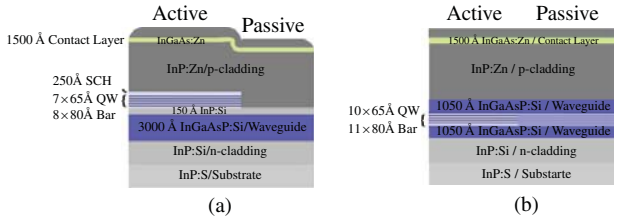


Fig. 2. (a) OQW and (b) CQW material platforms for high saturation power and high gain, respectively.

circuits (PICs) in this field. PICs offer a substantial cost reduction due to a greatly reduced system footprint, lower power consumption and packaging costs, and the possibility of performing many signal processing steps in the optical domain, thus avoiding the low-speed and power-hungry optical-to-electronic-to-optical (OEO) conversions [8], [9]. State-of-the-art PICs employing the above mentioned technologies for coherent-link applications have been recently reported in [6], [10], [13].

In this paper, we will overview recent advances in integrated photonic ICs for coherent communication and sensing applications within our research group at UCSB and present new results for each PIC. The development of PICs which take advantage of the compactness and phase stability of integrated optical waveguides to realize coherent building blocks for a wide range of applications will be included. In Section II, we describe the integration platform which we developed to monolithically integrate such building blocks. Afterwards, some examples will be given. First, efforts to create a digitally-controlled widely-tunable transmitter incorporating a widely-tunable laser together with an optical phase locked loop (OPLL) will be introduced. Details of this transmitter PIC layout and fabrication are given for the first time in this paper. Second, new results from compact optical comb generators to synthesize optical frequencies over a wide frequency range (5 THz) with a very high relative and absolute precision, will be given. These can be combined within the OPLL of the tunable transmitters to generate very wide bandwidth LIDAR waveforms [6]. Third, we will show how the small dimensions of a monolithic PIC can be taken advantage of to form a homodyne Costa's loop coherent receiver where the requirement for post-detection frequency and phase compensation to decouple the LO phase is eliminated. New measurement results are presented in Section V. Then in our fourth and final example, reconfigurable microwave signal processing devices are reviewed using compact, integrated ring-resonator based optical filters for analog coherent optical link applications. The progress on such filter work carried out at UCSB is shown and improved design and technology developed to improve the dynamic range are presented for the first time in Section VI.

## II. Integration Platform

Before diving into the details of each PIC, it is worth describing the technology that allows the monolithic integration of all the core active and passive components of our PICs in a high-yield, low-cost, and efficient way. This also demonstrates the strength and flexibility of the library of PICs for use as transmitters, receivers, and signal processing circuits for coherent optical links that we present in this paper.

Light sources, waveguide elements, modulators, amplifiers, phase shifters, and photodetectors were monolithically integrated in the PICs reported in this paper on two material platforms used at UCSB: offset quantum-well (OQW) and centered quantum-well (CQW) platforms, shown schematically in Figure 2. In the OQW active-passive platform, the multiple quantum-well (MQW) active layer is grown on top of the waveguide layer, which is common to active and passive components. The MQW layer is removed from the areas where passive components are desired and a single blanket regrowth of the upper cladding is finally performed on the wafer. The CQW active-passive configuration is similarly fabricated with an unpatterned cladding regrowth, but in this case the common waveguide contains the MQW-active region, and the bandgap of the MQW region has been selectively increased by a patterned implant and multiple annealing steps to selectively intermix the quantum-well barriers and wells in regions that are to become passive, or perhaps modulator sections, if the shift is not as large [14]. The CQW platform provides the highest confinement factor and gain per length, but also the lowest saturation power. As the QWs are moved away from the waveguide layer for OQW designs, the gain is reduced, while the saturation power is increased. We will discuss this technique further in Section VI.B. By incorporating both OQWs and CQWs, PICs can use both high gain semiconductor optical amplifiers (SOAs) for lasers and high saturation/linear SOAs. The integration is simply done by adding a regrowth step where the OQWs are grown on top of the CQW base-structure, in the intermixed region. The blanket cladding regrowth is then done as usual. In the same way, uni-travelling carrier (UTC) detectors can be integrated on the CQW platform for applications requiring high-speed photodetection. We have previously demonstrated such integration for wavelength converter and routing applications [9], [15]. For a more detailed description of these platforms, we refer to [8] and references therein.

Regardless which active-passive variation on the integration platform is chosen, the processing steps necessary to complete the PIC fabrication after regrowth are the same. More specifically, deeply etched waveguides are defined with photoresist

on a Cr/$SiO_2$ bilayer hardmask. The Cr is etched using a low power $Cl_2/O_2$(23.3 / 6.8 sccm) inductively coupled plasma (ICP) reactive ion etch (RIE) with 50 W applied to the ICP coil and 15 W on the substrate bias at a chamber pressure of 10 mT. The $SiO_2$ is etched using an $SF_6$/Ar (50 / 10 sccm) ICP-RIE with 600 / 50 W (ICP coil / substrate bias) at a chamber pressure of 7.5 mT. The $SiO_2$ to Cr selectivity is $>$30:1, and the etch chemistry provides a highly vertical etch of the silicon dioxide. The resulting 600 nm $SiO_2$ mask acts as a hardmask to define the InGaAsP/InP deeply etched waveguides using a $Cl_2/H_2$/Ar (9/18/2 sccm) ICP-RIE with 850 / 125W (ICP coil / substrate bias) at a chamber pressure of 1.5 mT and substrate temperature of 200 $^o$C [16]. Conventional III-V wet-etching techniques are used to integrate surface-ridge waveguides in the same chip when necessary, such as in large PICs that require both the small footprint offered by the deeply etched waveguides, and the reduced propagation losses and better heat dissipation of surface-ridge structures.

After removing the $SiO_2$ waveguide mask, blanket deposition of a 350 nm isolation layer of silicon nitride is performed. Vias are opened for topside p-metal contacts. N-metal contacts are realized through backside deposition of Ti/Pt/Au onto the n-doped conducting InP substrate or topside deposition on patterned vias when a semi-insulating (SI) substrate is needed (e.g. high-speed ICs).

Finally, a contact anneal at ~400 °C is performed in order to decrease the electrical resistance at the metal-semiconductor interface.

## III. Digitally-Synthesized Transmitters

The transition from analog to digital frequency synthesis mirror recent development in RF sources. Analog optical frequency synthesis uses a precisely tuned and controlled optical resonator to generate a target frequency. Digital optical frequency synthesis involves multiplication of fixed frequency reference oscillators to be able to precisely synthesize any optical frequency within a band of interest, such as the C-band. In this section we briefly introduce the scope of this work within the context of coherent links, and then we describe our approach for the realization of a digitally-synthesized transmitter IC using a low-linewidth laser and an RF reference.

Optical phase-locked loops are a key technology in the development of chip-scale generic integrated coherent transmitters that can be used for a variety of applications, such as terahertz frequency generation, coherent beam forming and high resolution frequency swept LIDAR sources [17], [18]. The resolution and range of frequency swept LIDAR systems are inversely proportional to the linearly chirped signal frequency bandwidth and laser linewidth, respectively. Sampled grating distributed Bragg reflector (SG-DBR) lasers, with their small footprint, 5 THz tuning range and high speed tuning, are ideal sources for $\mu$m resolution LIDAR [19]. An OPLL, in conjunction with an RF signal synthesizer, can be used to precisely and linearly control the frequency of the SG-DBR. Since the loop bandwidth of the feedback loop must be larger than the sum of the LO and reference laser, semiconductor lasers, e.g. SG-DBRs, with their large linewidths, require extremely short loop delays [6]. Monolithic integration along with custom built electronic circuits can enable an OPLL for heterodyne locking, realizing low linewidth, digitally synthesized THz dynamic range LIDAR sources.

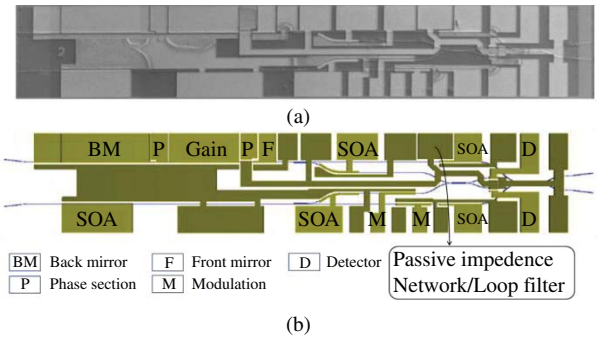


Fig. 3. (a) SEM image and (b) mask layout of design of an all-optical OPLL.

We have designed and fabricated a PIC with SG-DBR lasers, SOAs, 2 $\times$ 2 multi-mode interference (MMI) couplers, modulators and balanced detectors integrated on one chip, as shown in Figure 3. The PIC can be used in two configurations; one is all optical and uses a passive feedback loop to offset lock at a fixed frequency and the other uses custom designed electronics to synthesize a wavelength sweep. In the all optical design, both the LO and reference laser signals are split in a 1 $\times$ 2 MMI. At the MMI output, the LO is modulated by an RF source, mixed with half the reference power in a 2 $\times$ 2 MMI and detected by balanced detectors. The signal from the balanced detectors goes directly to the phase section of the SG-DBR, with a passive impedance network providing loop stability. This allows us to create an extremely low loop delay PLL. From the second MMI port, the LO signal mixed with the reference signal for optical output of the heterodyne signal. The unmixed LO signal, which will be used for LIDAR interrogation, can be coupled out from the back mirror of the SG-DBR.

These devices have been fabricated, however work toward a full LIDAR demonstration is still underway. In operation, to achieve a linear frequency sweep up to 5 THz, the SG-DBR LO can potentially be locked to a comb line from a wide bandwidth comb source, as shown in Figure 5. This is feasible as the linewidth of the comb source is comparable to the master SG-DBR used in the previous phase-locking experiment demonstrated in [6]. It is then possible to sweep the SG-DBR LO from one comb line to the next using a swept RF source applied to an electronic single sideband mixer in the feedback loop. Once it is within the loop bandwidth of the next comb line, the SG-DBR can then be locked to that line. Then, the RF sweep begins again, until the laser is swept over all the comb lines. The required bandwidth of the modulator and RF swept frequency source is only as large as the comb spacing.

These devices use the CQW platform described in Section II, and are processed on a SI InP:Fe substrate. Gratings were defined by electron-beam lithography before the p-cladding regrowth step. The integrated waveguides are both surface ridge (SR) for high power SG-DBRs and deep ridge (DR) for device compactness, incorporating a waveguide

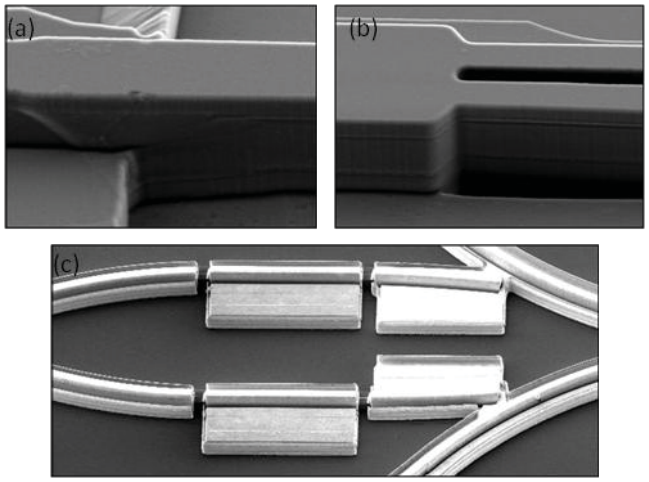


Fig. 4. SEM images of (a) surface ridge to deep ridge waveguide transition, (b) MMI lag etch at entrance of 2 × 2 MMI, and (c) Au He implant hardmask.

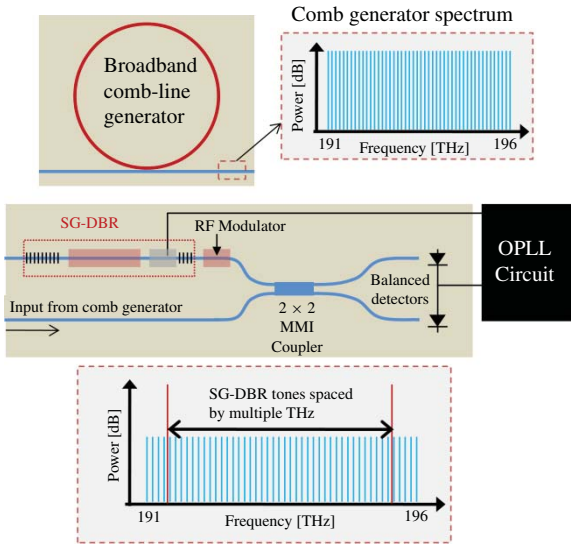


Fig. 5. LIDAR architecture showing comb generated from the ring mode-locked laser PIC at the top. In center, the SG-DBR laser is mixed with the comb generator signal in the 2-by-2 multimode interference coupler. The output from the optical mixing is measured on balanced detectors and the difference signal is fed back to the SG-DBR phase section, shifting the cavity frequency. This allows the OPLL circuit to track the incoming signal. RF modulation is added to the SG-DBR widely tunable laser for offset locking.

transition between them. Following regrowth, the ridge was defined using the bilayer Cr/SiO2 mask described earlier and etched for 1 $\mu$m everywhere. Then the DR sections were protected by PR and the SR sections were wet-etched. The SR sections were protected using a low temperature $SiO_2$ deposition and liftoff, and the DR sections were dry-etched using the chamber conditions described in section II. The entrance waveguides to the 2 × 2 MMIs need an additional etch step due to the RIE lag effect in which the etch rate is decreased drastically when waveguides are less than 1 $\mu$m apart. A $SiO_2$ mask is used to protect the ridge everywhere but the MMI regions, to avoid etching through the n-contact layer, and another dry etch is performed. After this, a n-mesa is created by wet etching and stopping on the n-InGaAs contact layer and n-metal is patterned via e-beam evaporation and liftoff. Next, a series of He implants, with the highest implant energy at 1675 keV, is used to create n-contact isolation between the balanced detectors. The hardmask process for the He implant consists of a two-stage angled Au deposition, with 2.5 $\mu$m of Au evaporated in each stage for a total of 5 $\mu$m in the planar regions, and is patterned via liftoff; this hardmask thickness is necessary to protect the waveguide from the high-energy implant [20]. The via openings for the n and p contacts are then formed as described in section II for a SI substrate. Several processing steps from the fabricated transmitter are shown in Figure 4.

## IV. Comb Generation in Coherent Links

### A. Broadband Phase-Locked Comb Applications

As discussed in the previous section, a broadband phase-locked frequency comb is very desirable for providing a reference grid for offset locking tunable lasers [6]. It can be also be used in a variety of other applications for coherent communication, such as a single cavity wavelength-division-multiplexing (WDM) source on the transmitter side [21], or multiple LOs on the receiver side. Enhanced performance could be expected from these latter examples if also combined with our recently demonstrated integrated optical phase-locked loops. For example, a coherent homodyne or heterodyne link using digital signal processing (DSP) would typically require each channel to have its own high-speed processing chip and a stable LO. The next generation of dense WDM grids spaced by 25 or 50 GHz with high spectral efficiency will contain 100 to 200 channels in the optical C-band. Thus as grid density increases, the required overhead to operate such a link with a DSP and an LO for each channel becomes quite costly, and the advantages realized from an integrated PIC with more functionality are apparent.

A 5 THz comb source with lines spaced by 25 GHz has the potential to replace 200 single frequency lasers with considerable savings in packaging and manufacture. Furthermore, with integrated OPLLs we can lock the frequency lines of the comb to the incoming signal avoiding the need for 200 DSP modules in a receiver array. If we use a phase-locked comb source on the transmitter side as well, only two OPLLs in the receiver are necessary to track the phase and frequency spacing. Phase locking combs to two frequency references for complete comb frequency stabilization has been studied extensively in fiber MLL based experiments [22]. As a result, by combining OPLLs and a compact broadband comb source we can reduce the overhead by as much as 200X. One potential drawback of the system, might be due to phase-noise, which can be significant at frequencies $<$1 GHz from acoustic phonon modes in long fiber links [23]. The interaction of phonon modes with phase-noise in this coherent systems is subject to many factors, and deserves careful examination, however it is outside the scope of this article.

MLLs typically consist of a laser cavity with a saturable absorber (SA) element. For semiconductor MLLs, an SA is fabricated using a reverse biased P-i-N junction of bulk, QW, or quantum-dot (QD) material. The SA becomes transparent

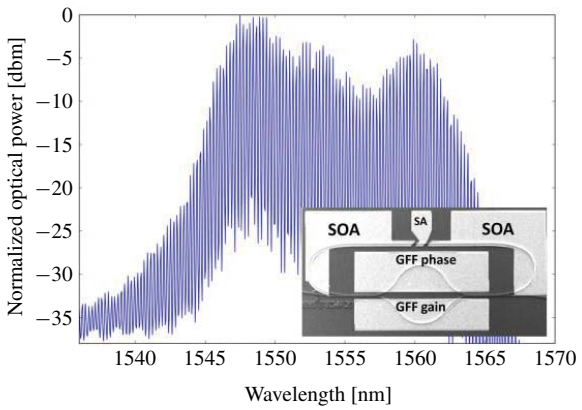


Fig. 6. Optical spectrum from gain flattened mode-locked laser. An SEM image of the GFF-MLL is shown in the inset. SOA: semiconductor optical amplifier. SA: saturable absorber. MZI: Mach-Zehnder interferometer.

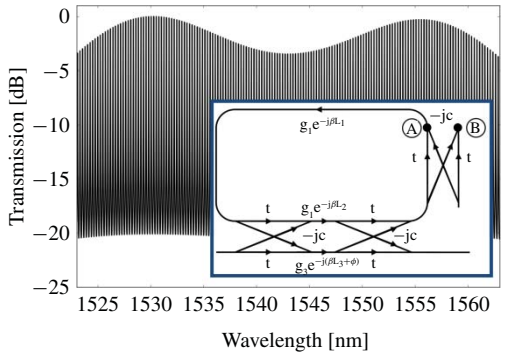


Fig. 7. Calculated output power response from a ring with a GFF. The inset shows the corresponding signal flow diagram where the power response taken from points A-to-B.

above a certain power, as carrier accumulation prevents further absorption of photons, providing less loss to narrower pulses with a high peak power. This mechanism shifts the cavity's lowest-loss operating state from continuous-wave (common in single-mode lasers) to periodic pulse-trains. A quick application of the Fourier transform, reveals that such temporal pulse-trains are only possible with multiple phase-locking frequency tones. Thus, phase-locked comb generation is the expected output from MLLs [24].

When combined with SG-DBR widely tunable lasers, the comb generator can be used to precisely place two tones at up to multiple THz intervals enabling RF generation and LIDAR. As shown in Figure 5, by applying RF modulation to the SG-DBR output before mixing with the comb, the laser can be offset locked from the discrete comb lines. When two of these lasers are mixed together, a beat tone is formed and broadband digital frequency sweeping becomes possible by adjusting the offset locked frequency.

### *B. Gain Flattening for Comb Generation*

In a semiconductor MLL, the span of the comb is determined by the cavity dispersion and the gain competition between its various lasing modes. While the semiconductor medium can generate gain that spans over 100 nm, the gain competition arising from the nonuniform material gain as a function of wavelength limits the bandwidth of the resulting frequency comb. We have overcome such limitations by introducing an intracavity filter with the inverse of the spectral shape of the material gain. Hence, the resulting net gain appears flattened, creating a more uniform spectral profile. This allows for wider comb generation as demonstrated with bench-top MLLs [25].

We have been pursuing some of the first work to incorporate a gain flattening filter (GFF) into integrated passively MLLs. With the intracavity filter enabled, the GFF-MLL shows significant improvement in pulse-width and comb span compared to similar rings without the filter [26], [27]. These GFF-MLLs produce the widest combs yet generated by integrated quantum-well based lasers with combs spanning more than 2 THz within their −10 dB bandwidth [28], as shown in Figure 6; this is more than 70 phase-locked lasing lines from a device with a footprint of 0.6 × 1.5 mm$^2$. This lasing span matches state-of-the art QD and quantum-dash MLLs [29]. These material platforms can provide an inherently flatter gain due to their nonuniform growth distribution, however reproducible QD gain spectra can be challenging as small growth changes can greatly alter the distribution of QDs. Moreover, such GFFs can be used to improve the gain flatness on any material platform, including: QDs, QWs, and bulk as future devices may require different semiconductor gain media.

The GFF-MLL is fabricated on the InGaAsP/InP offset quantum well (OQW) platform described in Section II. The active material is used to define SOAs and the SA, whereas the passive material is used to define the low-loss waveguides and current injection based phase shifters.

The fully fabricated GFF-MLL PIC has a round-trip cavity length of 2600 $\mu$m, corresponding to lasing lines spaced by 29.7 GHz, as shown in Figure 6. For offset locking SG-DBR tunable lasers or for use in WDM communication, 10-100 GHz frequency spacing is desired for the cavity modes. This requires ring circumferences to be ∼1 to 10 mm, making integrated cavities ideal for these applications. The 600 $\mu$m asymmetric MZI filter uses two 3 dB couplers with connecting arms that differ in length by 16 $\mu$m providing a free-spectral-range (FSR) of 40 nm. One of the arms of the MZI filter has an SOA that can be used to control the extinction ratio (ER) of the GFF, whereas the other arm has a phase shifter allowing adjustment of the filter center frequency. The optical power coupled into a lens fiber is −6 dBm. The measured −20 dB RF linewidth is <500 KHz and FWHM pulse-width is 900 fs [30]. Such linewidth and pulse-width measurements are consistent with other QW based passively mode-locked lasers [31], indicating that the gain flattening does not degrade phase-locking and moreover that hybrid mode-locking the cavity can be used to greatly reduce the linewidth further [32].

Using scattering matrix theory, we predict that further improvements in the GFF to achieve a 5 THz span are possible. As discussed in [28] and shown in the inset of Figure 7, the optimal filter has three 78% bar couplers, two of which are used for the filter, while the third serves as the output for the desired flattened response. The simulated output comb has

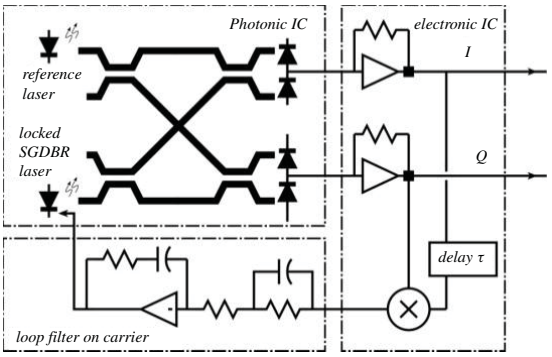


Fig. 8. Architecture of the coherent receiver showing three parts of this receiver: a photonic integrated circuit, an electrical integrated circuit, and a loop filter.

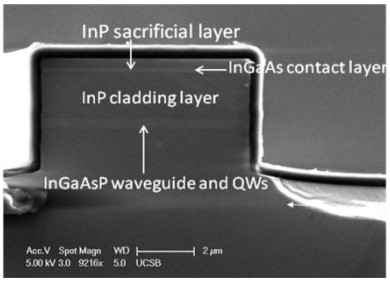


Fig. 9. Cross section of a waveguide.

a 3.5 dB power variation over its 40 nm operating window (see Figure 7). Therefore, while 2 THz bandwidths have been demonstrated on-chip, GFF-MLLs have the potential for comb generation spanning 5 THz or more.

## V. Coherent Receivers

As a part of optical coherent links, coherent optical receivers for digital communication applications have received a lot of interest recently. Compared to traditional direct detection receivers, coherent optical receivers have many advantages, such as higher detection sensitivity, greater tolerance to noise, compatibility with different modulation formats (such as multi-level phase shift keying or QAM), and their intrinsic ability to demultiplex wavelength-division multiplexed (WDM) channels without the use of optical filters [5], [33]–[36].

The most commonly used implementation of an optical coherent receiver is by using a free-running LO. Limited by laser linewidth and stability, high-speed digital signal processing is required to perform phase and frequency offset estimation and correction. However, the state-of-the-art high-speed digital signal processors that are used currently have high power consumption, limited speed and high cost.

One solution to this problem is to implement an optical phase-lock loop (OPLL) where an LO tracks the frequency and phase of the transmitter laser [6], [36], [37]. Although studies of optical phase-locked loops can be traced back almost fifty years, the OPLL has proven to be hard to implement. The main difficulty is that it requires a short loop delay and generally narrow linewidth lasers. For example, to achieve a 1 GHz loop bandwidth, the loop delay is normally required to be less than 100 ps. This is not feasible using fiber pigtailed components. However, by integrating all the photonic components monolithically, the footprint of the whole receiver becomes much smaller and therefore the loop delay can be significantly decreased.

To realize this phase-locked coherent receiver, we monolithically integrated a widely-tunable laser, a 90 degree hybrid and four high-speed photodetectors on an InGaAsP/InP-based photonic integrated chip. Besides the PIC, the receiver also includes an electrical integrated circuit (EIC) and a loop filter. The EIC is composed of two transimpedance amplifiers and an XOR gate. The loop filter is built on the carrier to provide more gain to the phase-locked loop and, more importantly, to introduce the correct filter function to keep the phase-locked loop stable. This architecture is shown in Figure 8. An integrated delay between I- and Q-data results in a DC component that is dependent on the frequency offset between input and LO laser, and provide frequency pull-in before the loop acquires phase-lock. Further, this architecture forms a Costa's loop, capable of coherent demodulation of BPSK modulated optical signals.

The PIC uses a widely-tunable SG-DBR laser [37] as the LO laser. Two variations of 90 degree hybrid designs are realized. One uses four MMI couplers, and the other uses a star coupler [38].

To monolithically integrate these optical components, we have used the InGaAsP/InP CQW platform presented in Section II, with an InP:S conducting substrate. The full epitaxial structure is shown in Figure 2, and Figure 9 is a SEM picture of a deeply etched waveguide cross section showing the epi layers. After quantum well intermixing, sampled gratings with a pitch size of 238 nm (shown in Figure 10(a)) are defined using electron beam lithography before the blanket regrowth of the p-cladding and InGaAs contact layer. For better laser performance and device compactness, we integrated both surface ridge waveguides and deeply etched waveguides on the same device with a low-loss waveguide transition between them, as previously described in Section III.

The $Cl_2/H_2/Ar$ based ICP-RIE dry etch resulted in very smooth ridge side walls and minimum undercut (Figure 10(b)) [16]. The surface ridge waveguide, the deeply etched waveguide, and the transition between them are shown in Figure 10(c).

Following the waveguide etching is the RF ground metal deposition and the bisbenzocyclobutene (BCB) definition steps. After that, the waveguide tops are opened for p-metal contacts followed by the opening of BCB vias for detectors and by our standard metal evaporation. In order to connect PIC and EIC by wire bonding, four 50-Ohm microstrip transmission lines are also fabricated on the PIC to bring all the signals from the photodetectors to the same side of the PIC. All the metal traces are 430 $\mu$m long and BCB is used as a dielectric layer. Figure 11(a) is the microscope picture of a PIC that is designed using MMI couplers as the 90 degree hybrid and Figure 11(b) shows the PIC that is designed using a star coupler.

The SG-DBR laser has been characterized. The output power is measured by an on-chip photodetector assuming unity

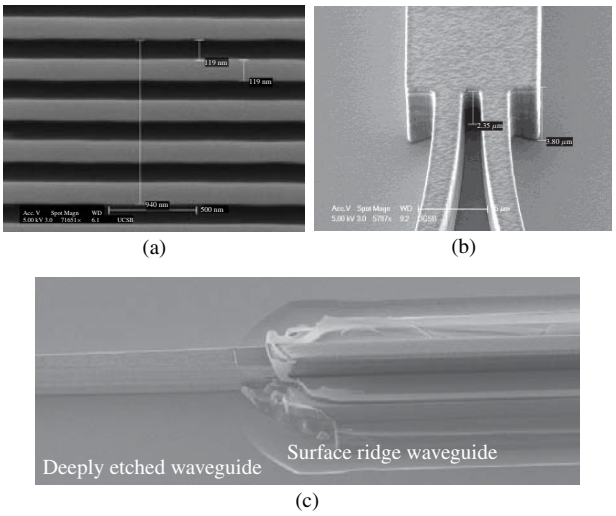


Fig. 10. SEM images of the fabricated PIC showing. (a) Gratings definition for SG-DBR lasers. (b) Vertical and smooth waveguide etch. (c) Waveguide transition from surface ridge to deeply etched waveguide. A linear tape is well designed to decrease the transition loss.

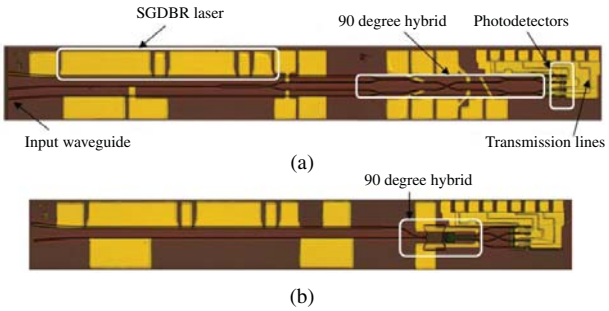


Fig. 11. Microscope images of the PIC showing. (a) PIC using MMI couplers as a 90 degree hybrid. (b) PIC using star coupler as a 90 degree hybrid.

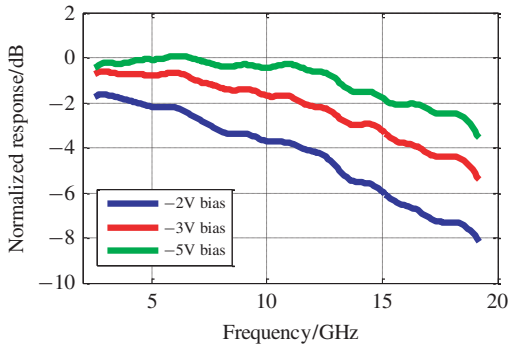


Fig. 12. Normalized frequency response of the photodetector with −2 V, −3 V, and −5 V DC bias.

quantum efficiency. The measured threshold current of the laser is around 40 mA and the maximum output optical power is 18 mW. A 40 nm tuning range has been achieved. The high-speed photodetector has also been tested. Figure 12 shows the relative frequency response of the detector with different DC biases. With a −5 V DC bias, an 18 GHz bandwidth can be achieved.

Back-to-back system characterization shows the functionality of the receiver without a phase-locked loop. The test

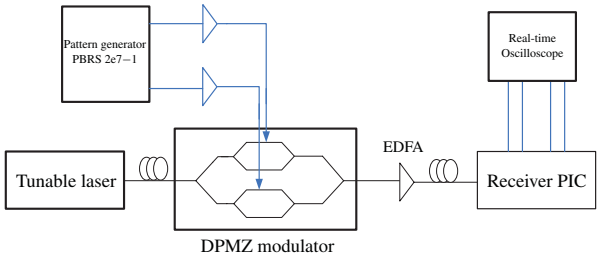


Fig. 13. Measurement setup for the coherent receiver.

setup is shown in Figure 13. Using the on-chip laser as an LO, the QPSK signal can be demodulated. The in-phase and quadrature data are detected on chip and sampled by a four-channel real-time oscilloscope. The sample rate is 40 GSa/s for each channel. While the measurements of the coherent receiver with an OPLL are currently being carried out, digital post-processing was performed offline on a computer for the first chip testing presented here in order to demonstrate the functionality of the coherent receiver PIC. The constellation diagram corresponding to a data rate of 10 Gb/s is shown in Figure 14.

## VI. High Dynamic Range PIC Filters for Coherent Analog Optical Links

### *A. Introduction and PIC Filter Results*

As mentioned in Section I, the power of coherent photonic systems extends beyond the digital telecom applications. Analog RF-photonic links can provide low-loss, very high bandwidth microwave transmission systems that are immune to electromagnetic interference [39]. Within analog photonic links, RF signal processing can be conducted in the optical domain. The wide-bandwidth nature of photonic systems opens the door to signal processing over bandwidths not attainable in RF electronics. In particular, microwave filtering in the optical domain can relieve demands placed on analog-digital converters or digital circuits normally tasked with performing the filtering application [40].

Recently, much attention has been given to photonic microwave filter PICs because of their size, weight, power, and stability improvements over bulk optical systems [41]-[46]. The optical stability provided by an integrated device allows for coherent signal processing of the optical signal. In this way, PICs can fulfill signal processing requirements for coherent optical links. In addition, process compatibility with the other components described in this paper allows for the integration of signal-processing functions on coherent link transmitter and receiver PICs, improving link functionality while reducing the total demands placed on digital post processing or electronic RF analog signal processing.

Integration on a direct-bandgap semiconductor material system like InGaAsP/InP provides design and operational flexibility because of the integration of SOAs on-chip. SOAs make it easier to produce high-quality filter shapes without introducing excess loss into the system [45]. They also provide a level of tunability and programmability not available in passive systems. When integrated with fast current-injection phase

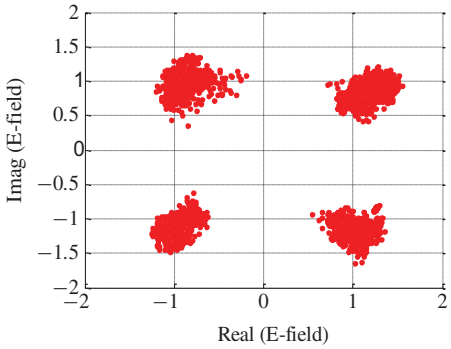


Fig. 14. Constellation diagram of the demodulated QPSK signal. The data rate is 10 Gb/s. Data are measured on a star-coupler-based device.

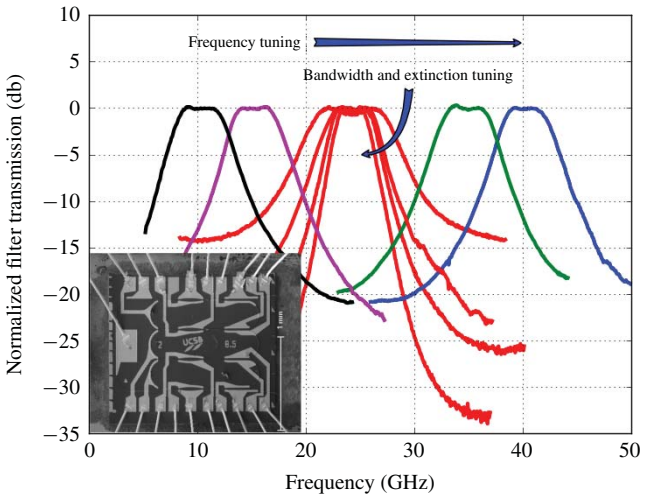


Fig. 15. Second-order coupled ring bandpass filters measured in the RF domain showing tunability in bandwidth and frequency. Filters are normalized to 0.0 dB passband gain for clarity, but have passband optical gain of 0–5 dB. The inset is an SEM image of a fabricated device. See [38] for more details on the device and measurement.

modulators, filters can be tuned in bandwidth and frequency in real-time. Recently, we fabricated and demonstrated cascaded [46] and coupled-ring [45] bandpass filters showing high levels of tunability and near-ideal filter shapes. Figure 15 shows the tuning capabilities of a $2^{nd}$ order coupled-ring bandpass filter. Coupled-ring structures easily synthesize bandpass filters whose bandwidth is controlled by the inter-ring coupling value. Pole magnitudes are set by the intra-ring SOAs [45]. The InGaAsP/InP material platform is also advantageous for monolithic integration with other link components like transmitters and receivers, as discussed in Section II.

While highly-tunable and high-quality filters were demonstrated, it is important that RF link performance not be compromised by the photonic subsystem. Integrated SOAs produce amplified-spontaneous-emission (ASE) noise and distortion via four-wave mixing that negatively impact the system spurious-free dynamic range (SFDR). The SFDR of a fabricated second-order bandpass filter was measured to be 86.3 dB-Hz$^{2/3}$, indicating the need for a high-dynamic-range design [46]. Such a design is achieved through the use of a high-saturation-power and low-loss material platform, and a high-SFDR device layout, as we discuss in the following sections B and C.

### B. High Dynamic Range SOAs

The noise and distortion that negatively impact the SFDR of an RF-photonic link incorporating a PIC filter originate in the integrated SOAs. ASE noise is generated in any SOA operating in the linear amplification regime, and in-band intermodulation distortion (IMD) is generated via carrier population oscillations that produce four-wave mixing [47]. The SFDR of a coherent link with an LO power much greater than all other optical powers can be written in terms of optical noise and third-order IMD output intercept point (OIP3) as [48],

$$SFDR = \left[\frac{P_{OIP3}}{S_{ASE} + \hbar\omega}\right]^{2/3}. \quad (1)$$

Where $S_{ASE}$ is the power spectral density of ASE in the mode, and $P_{OIP3}$ is the optical third-order IMD output intercept point. SFDR is given on a bandwidth-independent dB-Hz$^{2/3}$ scale. Using the definitions for $S_{ASE}$ and $P_{OIP3}$ from [48], we derive an equation for the SFDR of a single SOA in a link as

$$SFDR = \left[\frac{P_S G}{M[n_{sp}(G-1)/\varsigma + 1](G-1)}\right]^{2/3}. \quad (2)$$

Where $P_S$ is the SOA saturation power, $G$ is the single-pass power gain, $n_{sp}$ is the population inversion factor, and $\varsigma = (\Gamma g - \alpha_i)/\Gamma g$, where $\Gamma g$ is the modal gain, and $\alpha_i$ is the modal loss. For two closely spaced tones (the worst case), $M$ is a material parameter given by

$$M = \frac{\hbar\omega}{2}\sqrt{1 + \alpha^2/\varsigma^2}. \quad (3)$$

Where $\alpha$ is the linewidth enhancement factor and $\tau$ is the carrier lifetime. $M$ is constant for a certain material platform and for constant bias current. The SFDR of a system of many SOAs is a complex function of SOA gain and placement in the PIC, but (1) and (2) show that the best performance for an SOA is obtained at high current density, when $n_{sp}$ is small, $\zeta$ is close to 1, and saturation power is highest. Maximizing SFDR for a single SOA is equivalent to maximizing saturation power and minimizing total gain used. In a PIC, minimizing total gain used is equivalent to minimizing passive waveguide propagation loss and component insertion loss. If less loss is accrued, less gain is needed, and the structure achieves a higher SFDR. Thus, the key material attributes needed to achieve a high linearity integration platform are high $P_S$ and low loss.

We have fulfilled both these requirements by slightly modifying the well-established OQW material platform, previously described in the Section II of this paper. $P_S$ can be increased by lowering $\Gamma$ without reducing the active region cross section. This is done by inserting an extra InP layer in between the waveguide and the active region, there through lowering $\Gamma$. The penalty of increasing $P_s$ comes with trading off for lower modal gain, since $\Gamma$ is decreased. The lower gain is not a problem for our filter designs, which rely on reducing the incorporated SOA gain ($G$) to maximize SFDR ((1) and (2)). More importantly, having the CT-layer in the passive sections exponentially reduces the propagation loss since the modal overlap with the p-cladding and thus the inter-valence band absorption is reduced [49]. Figure 16 schematically illustrates this integration platform, with the key CT-layer highlighted.

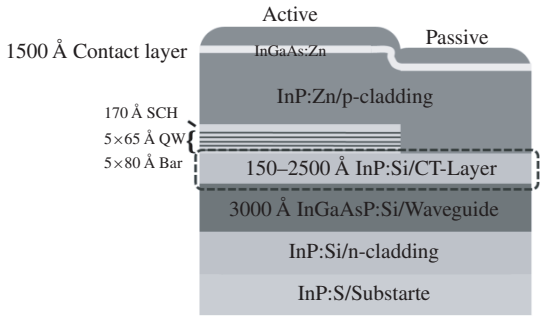


Fig. 16. Schematic illustration of the InGaAsP high dynamic range platform for active/passive device integration.

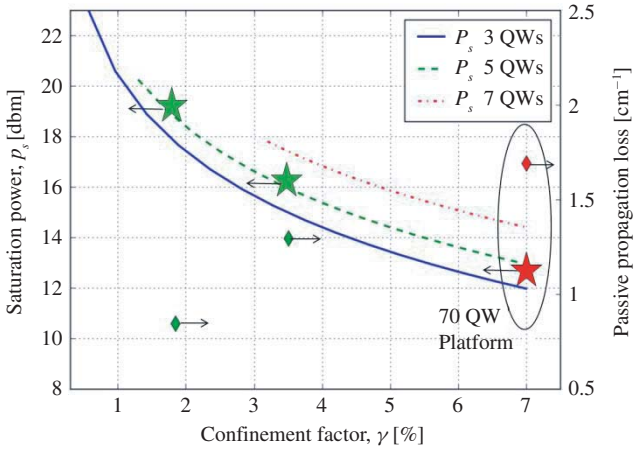


Fig. 17. Simulated $P_S$ as a function of $\Gamma$, varying number of QWs and CT-layer thickness (lines). Superimposed with measured output saturation powers (stars), and averaged passive losses (diamonds) for corresponding CT-layer designs. For the passive loss measurement, the standard deviation is $<0.087$ cm$^{-1}$ for all points. The standard OQW with 7QWs is highlighted for reference.

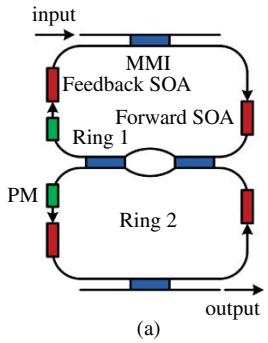


(a)

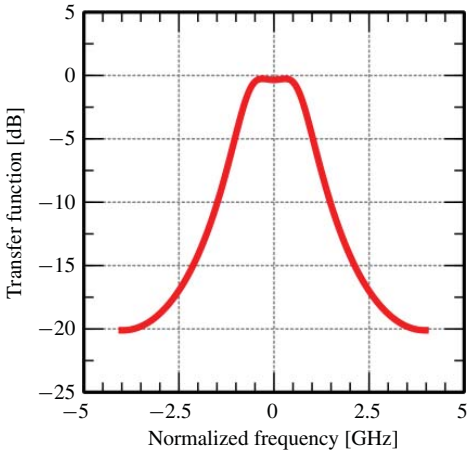


(b)

Fig. 18. (a) Schematic representation of a second-order coupled ring filter. MMIs are in blue, SOAs in red, and phase modulators (PM) in green. The inter-ring coupling value is controlled by the Mach-Zehnder interferometer (MZI) tunable coupler comprised of two MMIs and two waveguides of equal length. (b) Simulated transfer function of a second-order coupled ring bandpass filter with inter-ring coupling of 15%. This optimal-SFDR filter provides a passband gain of $-0.26$ dB.

One boundary condition for the CT-layer technique is that the CT-layer cannot be made too thick, such that higher order transverse modes are guided. This effectively limits the number of wells that can be used for a given $P_S$, and is manifested by the broken lines in the simulation of $P_S$ in Figure 17. The active/passive integration for this platform is analogous to the standard OQW platform, with a simple wet-etch step removing the quantum wells in passive sections, and a single blanket regrowth of the p-cladding. We have characterized this high linearity platform using a deeply etched waveguide design. The deep etching allows for maximum flexibility in device integration since the mode has large lateral confinement and the dry etch fabrication does not require a specific crystallographic direction. The filter PICs described previously use deeply etched waveguides.

Figure 17 shows the measured output saturation power and passive loss for a few different $\Gamma$ designs. The measured results match theory very well; $P_S$ increases and passive loss decreases with decreasing $\Gamma$ (increasing CT-layer thickness). The loss with the lowest confinement OQW design is 0.34dB/mm, improved by factor over the standard OQW design. At the same time, $P_S$ was improved by $>7$dB to 19.1dBm, this is the highest reported$P_S$ to our knowledge using $\leq 3\mu$m wide waveguides. The gain for this design is measured to be 7.8 dB/mm, which is sufficient to balance the accrued loss in our PIC filters. The proven loss and saturation improvements for the OQW platform promise to facilitate high dynamic range PIC filters, which will be discussed in the next section.

As mentioned in the end of the Integration Platform section, it is fully possible to integrate high-gain CQW sections with these high-linearity SOA structures, simply by adding a second regrowth. This way an LO laser and balanced receiver could be integrated with the RF-filter application.

### *C. Next Generation High Dynamic Range Microwave PIC Filters*

In [48], we develop a model to calculate the SFDR of an arbitrary PIC system with SOAs operating in the linear amplification regime. ASE and IMD are calculated for each SOA, and their contributions summed at the receiver depending on the frequency-dependent transfer function from the PIC input to the SOA, and from the SOA to the PIC output. This model creates a method for investigating the impacts of device design on SFDR.

In addition to the importance of integration on a high-saturation-power material platform proven in the last section, the layout of a signal-processing PIC is crucial for obtaining

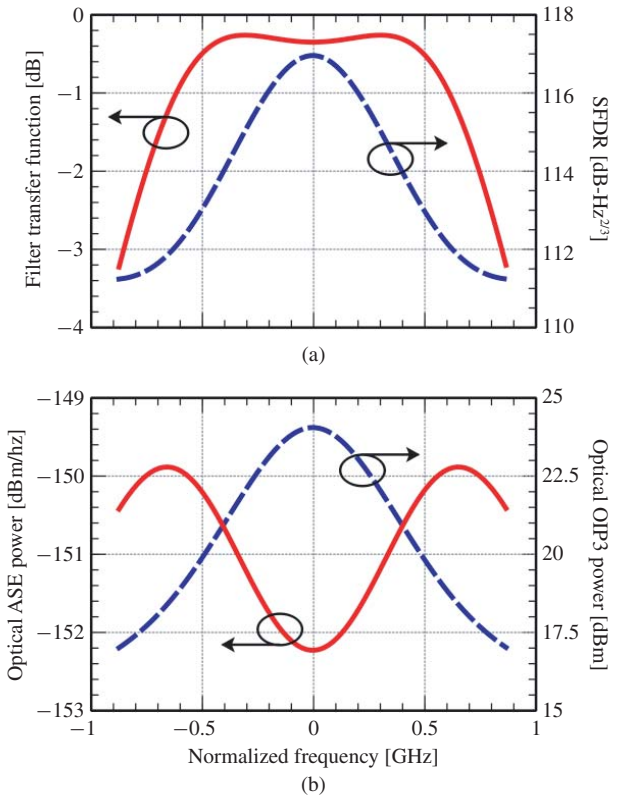


Fig. 19. (a) Simulated transfer function and SFDR over the 3 dB bandwidth of the SFDR-optimal second-order coupled ring bandpass filter. (b) Simulated ASE noise output and OIP3 power over the 3 dB bandwidth at the output of the same filter.

high SFDR. Here, we will use a second-order coupled ring bandpass filter as an example to demonstrate the design process.

The second-order coupled-ring filter shown in Figure 18(a) produces two transfer function poles, the magnitudes of which are set by the net ring gain and loss. The phases of the poles are set by the round-trip phase accumulation, and are tuned by the phase modulators. When the two ring resonances are located at the same frequency, the coupled nature of the transfer function causes the poles to split in frequency. The frequency separation is determined by the magnitude of the inter-ring coupling. As inter-ring coupling increases, the poles move away from each other and the filter bandwidth increases. By appropriately setting the pole magnitudes and inter-ring coupling value, a flat-topped bandpass filter can be synthesized. An example of this flat-topped filter is shown in Figure 18(b).

The pole magnitudes used to create the filter shape are dependent on the total gain and loss in the ring, but not on the location of that gain and loss. For example, SOA gain can be located either in the "feedback" or "forward" waveguide segments as shown in Figure 18(a). By adjusting the distribution of gain between these forward and feedback segments, the filter transfer function will move up and down on a dB scale, while the filter shape remains the same. In this way, the filter can be designed for a specific passband gain. As the SOA distributions are changed, the SFDR will also vary. It is also crucial for high SFDR to locate all SOAs at the end of their respective waveguide segments in order to minimize signal power (and hence distortion generation) in the SOAs [48].

For this filter, the optimal SFDR is obtained when the ring 1 SOA is located in the feedback segment, and the ring 2 SOA is located in the forward segment. Figure 19 shows the transfer function, SFDR, ASE, and OIP3 power as a function of frequency over the 3 dB bandwidth for this arrangement. The model uses the measured results presented in Section VI-B to calculate the SFDR of a device fabricated on the high-saturation-power integration platform. An SFDR range of 111.2–117.0 dB-Hz$^{2/3}$ is predicted over the 3dB filter bandwidth. ASE power and IMD are higher at the edges of the passband (OIP3 is lower) causing a degradation of SFDR in those areas. The SFDR of an arbitrary signal in the passband is a complex function of many-tone interactions, but the SFDR range reported here provides and upper and lower bound [48].

The PIC-limited SFDR calculated with this model is comparable to recent measurements of coherent RF-photonic links incorporating passive microwave photonic filters [50], [51]. Importantly, active PIC filters like the example in Figure 19 do not have insertion loss, which can relieve demands on the transmitter and receiver. With the possibility to monolithically integrate PIC filters with a transmitter or receiver, the active InGaAsP/InP material system is attractive for use in next-generation coherent RF-photonic links.

## VII. Conclusion

We have demonstrated photonic circuits monolithically integrated on an InP-based platform for use in coherent communication links. We have shown examples of an integrated transmitter that uses an optical phase locked loop to both accurately set the wavelength as well as possibly narrow the linewidth. Compatible mode-locked ring lasers are illustrated as possible on-chip WDM sources, which have been demonstrated with a flat gain profile across a 2 THz band. New device designs promise to provide a flatted gain over a 5 THz band. We have shown coherent receivers incorporating an integrated widely tunable laser: open-loop measurements demonstrated a 10 Gb/s QPSK transmission. Paired with an OPLL, the coherent receiver has the potential to demonstrate phase-locked operation without DSP post-processing. This is a preferable solution especially for short-haul links where dispersion is less of an issue, since our OPLL offers an easier and more power-efficient integration. Finally a tunable, programmable optical bandpass filter for use in analog coherent RF links is demonstrated. With an established higher-saturation and lower-loss OQW design, improved filter designs can potentially exceed 117 dB-Hz$^{2/3}$ SFDR.

## Acknowledgment

The authors would like to thank the many former and present University of California, Santa Barbara, students and colleagues that have performed much of the work presented herein and especially the collaboration of J. E. Bowers on much of the research.

## REFERENCES


[1] A. J. Rogers, "Polarization-optical time domain reflectometry: A technique for the measurement of field distributions," *Appl. Opt.*, vol. 20, no. 6, pp. 1060–1074, 1981.

[2] Cisco Systems. (2011, Jun.). *Visual Networking Index*, San Jose, CA [Online]. Available: http://www.cisco.com

[3] M. Nakazawa, K. Kikuchi, and T. Miyazaki, *High Spectral Density Optical Communication Technolgies*, vol. 6. Berlin, Germany: Springer-Verlag, 2010, pp. 103–127.

[4] P. Magill, "100 Gigabit Ethernet from a carrier's perspective," in *Proc. IEEE Lasers Electro-Opt. Soc. Ann. Meet.*, Lake Buena Vista, FL, Oct. 2007, pp. 21–25.

[5] R.-J. Essiambre, G. Kramer, P. J. Winzer, G. J. Foschini, and B. Goebel, "Capacity limits of optical fiber networks," *J. Lightw. Techol.*, vol. 28, no. 4, pp. 662–701, Feb. 2010.

[6] S. Ristic, A. Bhardwaj, M. J. Rodwell, L. A. Coldren, and L. A. Johansson, "An optical phase-locked loop photonic integrated circuit," *J. Lightw. Technol.*, vol. 28, no. 4, pp. 526–538, Feb. 2010.

[7] K. Iiyama, W. Lu-Tang, and H. Ken-Ichi, "Linearizing optical frequency-sweep of a laser diode for FMCW reflectometry," *IEEE J. Lightw. Technol.*, vol. 14, no. 2, pp. 173–178, Feb. 1996.

[8] L. A. Coldren, S. C. Nicholes, L. Johansson, S. Ristic, R. S. Guzzon, E. J. Norberg, and U. Krishnamachari, "High performance InP-based photonic ICs-A tutorial," *IEEE J. Lightw. Technol.*, vol. 29, no. 4, pp. 554–570, Feb. 2011.

[9] S. C. Nicholes, M. L. Masanovic, B. Jevremovic, E. Lively, L. A. Coldren, and D. J. Blumenthal, "An 8×8 InP monolithic tunable optical router (MOTOR) packet forwarding chip," *IEEE J. Lightw. Technol.*, vol. 28, no. 4, pp. 641–650, Feb. 2010.

[10] R. Nagarajan, J. Rahn, M. Kato, J. Pleumeekers, and D. Lambert, "10 channel, 45.6 Gb/s per channel, polarization multiplexed DQPSK, InP receiver photonic integrated circuit," *IEEE J. Lightw. Technol.*, vol. 29, no. 4, pp. 386–395, Feb. 2011.

[11] P. Evans, M. Fisher, R. Malendevich, A. James, P. Studenkov, G. Goldfarb, T. Vallaitis, M. Kato, P. Samra, S. Corzine, E. Strzelecka, R. Salvatore, F. Sedgwick, M. Kuntz, V. Lal, D. Lambert, A. Dentai, D. Pavinski, B. Behnia, J. Bostak, V. Dominic, A. Nilsson, B. Taylor, J. Rahn, S. Sanders, H. Sun, K.-T. Wu, J. Pleumeekers, R. Muthiah, M. Missey, R. Schneider, J. Stewart, M. Reffle, T. Butrie, R. Nagarajan, C. Joyner, M. Ziari, F. Kish, and D. Welch, "Multi-channel coherent PM-QPSK InP transmitter photonic integrated cirtuit (PIC) operating at 112 Gb/s Per wavelength," in *Proc. Opt. Fiber Commun. Conf.*, Los Angeles, CA, Mar. 2011, pp. 1–3.

[12] L. Johansson, U. Krishnamachari, A. Ramaswamy, J. Klamkin, S. Ristic, H.-F. Chou, L. A. Coldren, M. Rodwell, and J. E. Bowers, "Linear coherent optical receivers," in *Proc. Opt. Fiber Commun. Conf.*, San Diego, CA, Mar. 2010, pp. 1–3.

[13] E. J. Norberg, R. S. Guzzon, J. S. Parker, L. A. Johansson, and L. A. Coldren, "Programmable photonic microwave filters monolithically integrated in InP-InGaAsP," *IEEE J. Lightw. Technol.*, vol. 29, no. 11, pp. 1611–1619, Jun. 2011.

[14] E. J. Skogen, J. S. Barton, S. P. Denbaars, and L. A. Coldren, "A quantum-well-intermixing process for wavelength-agile photonic integrated circuits," *IEEE J. Sel. Topics Quantum Electron.*, vol. 8, no. 4, pp. 863–869, Jul.–Aug. 2002.

[15] J. W. Raring, M. N. Sysak, A. T. Pedretti, M. Dummer, E. J. Skogen, J. S. Barton, S. P. Denbaars, and L. A. Coldren, "Advanced integration schemes for high-functionality/high-performance photonic integrated circuits," *Proc. SPIE*, vol. 6126, pp. 1–12, Jan. 2006.

[16] J. S. Parker, E. J. Norberg, R. S. Guzzon, S. C. Nicholes, and L. A. Coldren, "High verticality InP/InGaAsP etching in $Cl_2/H_2/Ar$ inductively coupled plasma for photonic integrated circuits," *J. Vac. Sci. Technol. B*, vol. 29, no. 1, pp. 011016-1–011020-5, 2011.

[17] L. Ponnampalam, M. J. Fice, F. Pozzi, C. C. Renaud, D. C. Rogers, I. F. Lealman, D. G. Moodie, P. J. Cannard, C. Lynch, L. Johnston, M. J. Robertson, R. Cronin, L. Pavlovic, L. Naglic, M. Vidmar, and A. J. Seeds, "Monolithically integrated photonic heterodyne system," *J. Lightw. Technol.*, vol. 29, no. 15, pp. 2229–2234, Aug. 2011.

[18] N. Satyan, A. Vasilyev, G. Rakuljic, V. Levya, and A. Yariv, "Precise control of broadband frequency chirps using optoelectronic feedback," *Opt. Exp.*, vol. 17, no. 18, pp. 15991–15999, 2009.

[19] L. A. Coldren, "Monolithic tunable diode lasers," *IEEE J. Sel. Topics Quantum Electron.*, vol. 6, no. 6, pp. 988–999, Nov.–Dec. 2000.

[20] J. Klamkin, J. M. Hutchinson, J. T. Getty, L. A. Johansson, E. J. Skogen, and L. A. Coldren, "High efficiency widely tunable SGDBR lasers for improved direct modulation performance," *IEEE J. Sel. Topics Quantum Electron.*, vol. 11, no. 5, pp. 931–938, Sep.–Oct. 2005.

[21] Y. B. M'Sallem, Q. T. Le, L. Bramerie, Q. Nguyen, E. Borgne, P. Besnard, A. Shen, F. Lelarge, S. LaRochelle, L. A. Rusch, and J. Simon, "Quantum-dash mode-locked laser as a source for 56-Gb/s DQPSK modulation in WDM multicast applications," *IEEE Photon. Technol. Lett.*, vol. 23, no. 7, pp. 453–455, Apr. 2011.

[22] B. R. Washburn, S. A. Diddams, N. R. Newbury, J. W. Nicholson, M. F. Yan, and C. G. Jrgensen, "Phase-locked, erbium-fiber-laser-based frequency comb in the near infrared," *Opt. Lett.*, vol. 29, no. 3, pp. 250–252, 2004.

[23] K. Blotekjaer, "Thermal noise in optical fibers and its influence on long-distance coherent communication systems," *J. Lightw. Technol.*, vol. 10, no. 1, pp. 36–41, Jan. 1992.

[24] P. J. Delfyett, S. Gee, M. T. Choi, H. Izadpanah, W. Lee, S. Ozharar, F. Quinlan, and T. Yilmaz, "Optical frequency combs from semiconductor lasers and applications in ultrawideband signal processing and communications," *J. Lightw. Technol.*, vol. 24, no. 7, pp. 2701–2719, Jul. 2006.

[25] M. M. Mielke, G. A. Alphonse, and P. J. Delfyett, "Multiwavelength modelocked semiconductor lasers for photonic access network applications," *IEEE J. Sel. Areas Commun.*, vol. 25, no. 3, pp. 120–128, Apr. 2007.

[26] J. S. Parker, A. Bhardwaj, P. R. A. Binetti, Y.-J. Hung, C. Lin, and L. A. Coldren, "Integrated 30 GHz passive ring mode-locked laser with gain flattening filter," in *Proc. IEEE Int. Semiconduct. Laser Conf.*, Kyoto, Japan, Sep. 2010, pp. 1–2.

[27] J. S. Parker, P. R. A. Binetti, A. Bhardwaj, R. S. Guzzon, E. J. Norberg, Y. Hung, and L. A. Coldren, "Comparison of comb-line generation from InGaAsP/InP integrated ring mode-locked lasers," in *Proc. Lasers Electro-Opt.*, Baltimore, MD, May 2011, pp. 1–2.

[28] J. S. Parker, R. S. Guzzon, E. J. Norberg, A. Bhardwaj, P. R. A. Binetti, and L. A. Coldren, "Theory and design of intracavity gain-flattening filter for monolithically integrated mode–locked lasers," *IEEE J. Quantum Electron.*, vol. 48, no. 3, p. 1, Nov. 2011.

[29] J. P. Tourrenc, A. Akrout, K. Merghem, A. Martinez, F. Lelarge, A. Shen, G. H. Duan, and A. Ramdane, "Experimental investigation of the timing jitter in self-pulsating quantum-dash lasers operating at 1.55 $\mu$m," *Opt. Exp.*, vol. 16, no. 22, pp. 17706–17713, 2008.

[30] J. S. Parker, A. Bhardwaj, P. R. A. Binetti, and L. A. Coldren, "Monolithically integrated gain flattened mode-locked laser for comb-line generation," *IEEE Photon. Technol. Lett.*, 2011, to be published.

[31] K. Merghem, A. Akrout, A. Martinez, G. Moreau, J.-P. Tourrenc, F. Lelarge, F. Van Dijk, G.-H. Duan, G. Aubin, and A. Ramdane, "Short pulse generation using a passively mode locked single InGaAsP/InP quantum well laser," *Opt. Exp.*, vol. 16, no. 14, pp. 10675–10683, 2008.

[32] B. R. Koch, A. W. Fang, O. Cohen, and J. E. Bowers, "Mode-locked silicon evanescent lasers," *Opt. Exp.*, vol. 15, no. 18, pp. 11225–11233, 2007.

[33] F. Derr, "Coherent optical QPSK intradyne system: Concept and digital receiver realization," *J. Lightw. Technol.*, vol. 10, no. 9, pp. 1290–1296, 1992.

[34] R. Nagarajan, D. Lambert, M. Kato, V. Lal, G. Goldfarb, J. Rahn, M. Kuntz, J. Pleumeekers, A. Dentai, H.-S. Tsai, R. Malendevich, M. Missey, K.-T. Wu, H. Sun, J. McNicol, J. Tang, J. Zhang, T. Butrie, A. Nilsson, M. Reffle, F. Kish, and D. Welch, "10 channel, 100 Gbit/s per channel, dual polarization, coherent QPSK, monolithic InP receiver photonic integrated circuit," in *Proc. Opt. Fiber Commun. Conf.*, Los Angeles, CA, Mar. 2011, pp. 1–3.

[35] A. Beling, N. Ebel, A. Matiss, G. Unterbörsch, M. Nölle, J. K. Fischer, J. Hilt, L. Molle, C. Schubert, F. Verluise, and L. Fulop, "Fully-integrated polarization-diversity coherent receiver module for 100 G DP-QPSK," in *Proc. Opt. Fiber Commun. Conf.*, Los Angeles, CA, Mar. 2011, pp. 1–3.

[36] M. J. Fice, A. Chiuchiarelli, E. Ciaramella, and A. J. Seeds, "Homodyne coherent optical receiver using an optical injection phase-lock loop," *IEEE J. Lightw. Technol.*, vol. 29, no. 8, pp. 1152–1164, Apr. 2011.

[37] M. Lu, A. Bhardwaj, A. Sivananthan, L. A. Johansson, H. Park, E. Bloch, M. J. Rodwell, and L. A. Coldren, "Widely-tunable integrated coherent optical receiver using a phase-locked loop," in *Proc. IEEE Photon. Conf.*, Arlington, VA, Oct. 2011, no. ThL4.

[38] C. R. Doerr, M. D. Gill, A. H. Gnauck, L. L. Buhl, P. J. Winzer, M. A. Cappuzzo, A. Wong-Foy, E. Y. Chen, and L. T. Gomez, "Monolithic demodulator for 40-Gb/s DQPSK using a star coupler," *IEEE J. Lightw. Technol.*, vol. 24, no. 1, pp. 171–174, Jan. 2006.

[39] J. Yao, "Microwave photonics," *IEEE J. Lightw. Technol.*, vol. 27, no. 3, pp. 314–335, Feb. 2009.

[40] J. Capmany, B. Ortega, and D. Pastor, "A tutorial on microwave photonic filters," *IEEE J. Lightw. Technol.*, vol. 24, no. 1, pp. 201–229, Jan. 2006.

[41] M. S. Rasras, D. M. Gill, S. S. Patel, K.-Y. Tu, Y.-K. Chen, A. E. White, A. T. S. Pomerene, D. N. Carothers, M. J. Grove, D. K. Sparacin, J. Michel, M. A. Beals, and L. C. Kimerling, "Demonstration of a fourth-order pole-zero optical filter integrated using CMOS processes," *IEEE J. Lightw. Technol.*, vol. 25, no. 1, pp. 87–92, Jan. 2007.

[42] N.-N. Feng, P. Dong, D. Feng, W. Qian, H. Liang, D. C. Lee, J. B. Luff, A. Agarwal, T. Banwell, R. Menendez, P. Toliver, T. K. Woodward, and M. Asghari, "Thermally-efficient reconfigurable narrowband RF-photonic filter," *Opt. Exp.*, vol. 18, no. 24, pp. 648–24 653, Nov. 2010.

[43] P. Dong, N.-N. Feng, D. Feng, W. Qian, H. Liang, D. C. Lee, B. J. Luff, T. Banwell, A. Agarwal, P. Toliver, R. Menendez, T. K. Woodward, and M. Asghari, "Ghz-bandwidth optical filters based on high-order silicon ring resonators," *Opt. Exp.*, vol. 18, no. 23, pp. 23784–23789, Nov. 2010.

[44] H.-W. Chen, A. Fang, J. D. Peters, Z. Wang, J. Bovington, D. Liang, and J. Bowers, "Integrated microwave photonic filter on a hybrid silicon platform," *IEEE Trans. Microw. Theory Tech.*, vol. 58, no. 11, pp. 3213–3219, Nov. 2010.

[45] R. S. Guzzon, E. J. Norberg, J. S. Parker, L. A. Johansson, and L. A. Coldren, "Integrated InP-InGaAsP tunable coupled ring optical bandpass filters with zero insertion loss," *Opt. Exp.*, vol. 19, no. 8, pp. 7816–7826, 2011.

[46] E. J. Norberg, R. S. Guzzon, J. Parker, L. A. Johansson, and L. A. Coldren, "Programmable photonic microwave filters monolithically integrated in InP/InGaAsP," *IEEE J. Lightw. Technol.*, vol. 29, no. 11, pp. 1611–1619, Jun. 2011.

[47] G. P. Agrawal, "Population pulsations and nondegenerate four-wave mixing in semiconductor lasers and amplifiers," *J. Opt. Soc. Amer. B*, vol. 5, no. 1, pp. 147–159, Jan. 1988.

[48] R. S. Guzzon, E. J. Norberg, and L. A. Coldren, "Spurious-free dynamic range in photonic integrated circuit filters with semiconductor optical amplifiers," *IEEE J. Quantum Electron.*, 2011, to be published.

[49] E. J. Norberg, R. S. Guzzon, and L. A. Coldren, "An InGaAsP/InP integration platform with low loss deeply etched waveguides and record SOA RF-linearity," in *Proc. Eur. Conf. Opt. Commun.*, Geneva, Switzerland, 2011, pp. 1–3.

[50] K.-Y. Tu, M. S. Rasras, D. M. Gill, S. S. Patel, Y.-K. Chen, A. E. White, A. Pomerene, D. Carothers, J. Beattie, M. Beals, J. Michel, and L. C. Kimerling, "Silicon RF-photonic filter and down-converter," *IEEE J. Lightw. Technol.*, vol. 28, no. 20, pp. 3019–3028, Oct. 2010.

[51] A. Agarwal, T. Banwell, and T. Woodward, "Optically filtered microwave photonic links for RF signal processing applications," *IEEE J. Lightw. Technol.*, vol. 29, no. 16, pp. 2394–2401, Aug. 2011.

**Pietro R. A. Binetti** received the Ph.D. degree in electrical engineering from COBRA Research Institute, Eindhoven University of Technology, Eindhoven, The Netherlands, in 2009.

He is currently a Post-Doctoral Fellow with the University of California, Santa Barbara. His current research interests include design, fabrication, and characterization of photonic integrated circuits for analog and digital applications.

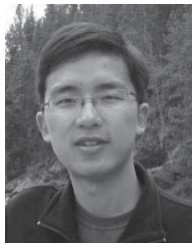

**Mingzhi Lu** received the B.S. degree in electrical engineering from Southeast University, Nanjing, China, in 2008. He is currently pursuing the Ph.D. degree in electrical engineering with the University of California, Santa Barbara.

His past research experience includes microwave and THz frequency selective surfaces and metamaterials. His current research interests include InGaAsP/InP based photonic integrated coherent receivers and optical phase-locked loops.

**Erik J. Norberg** received the B.S. and M.S. degrees in engineering nanoscience from Lund University, Lund, Sweden, in 2008. He is currently pursuing the Ph.D. degree in electrical engineering with the University of California, Santa Barbara.

He is currently working on the development of high dynamic range integrated optical filters for microwave signal processing. His current research interests include design and metal organic chemical vapor deposition growth of large scale photonic integrated circuits on InP.

**Robert S. Guzzon** received the B.S. degree in electrical engineering and physics from Lehigh University, Bethlehem, PA, in 2007. He is currently pursuing the Ph.D. degree in electrical engineering with the University of California, Santa Barbara.

His current work focuses on the design and fabrication of versatile photonic integrated microwave filter systems that achieve high spurious-free dynamic range. His current research interests include large-scale photonic integration, particularly applied to microwave photonic signal processing.

**John S. Parker** received the B.S. degree in engineering from Harvey Mudd College, Claremont, CA, in 2007, and the M.S. degree in electrical and computer engineering from the University of California, Santa Barbara, in 2009, where he is currently pursuing the Ph.D. degree.

His current research interests include radio frequency photonics, coherent communication, and compact components for dense photonic integrated circuits.

**Abirami Sivananthan** received the B.S. degree in engineering physics from the University of Illinois at Urbana-Champaign, Urbana, in 2007, and the M.S. degree in electrical and computer engineering from the University of California, Santa Barbara, in 2009. She is currently pursuing the Ph.D. degree in electrical engineering with the University of California.

Her current research interests include optical phase locked loops to achieve low linewidth semiconductor lasers and widely tunable photonic integrated transmitters on the InGaAsP/InP integration platform.

**Ashish Bhardwaj** received the B.Sc. (honors) and M.Sc. degrees in physics from the Indian Institute of Technology, Kharagpur, India, in 1994 and 1996, respectively, and the Ph.D. degree in applied physics from the California Institute of Technology, Pasadena, in 2001.

He was with Bell Laboratories, Lucent Technologies, Holmdel, NJ, from 2001 to 2007, as a Technical Staff Member, where he was engaged in research on fast wavelength switching in tunable lasers for applications in optical packet switching. He also led research in the design, fabrication, and characterization of large-scale monolithically integrated InP-based photonic integrated circuits employing semiconductor optical amplifiers. From 2007 to 2011, he was with the Department of Electrical and Computer Engineering, University of California, Santa Barbara, where he led research in the design and fabrication of monolithically integrated optical phase locked loops as coherent receivers for high dyamic range radio frequency/photonic links. He is currently with JDS Uniphase Corporation, San Jose, CA.

**Leif A. Johansson** (M'04) received the Ph.D. degree in engineering from University College London, London, U.K., in 2002.

He is currently a Research Scientist with the University of California, Santa Barbara. His current research interests include design and characterization of integrated photonic devices for analog and digital applications and analog photonic systems and subsystems.

**Mark J. Rodwell** (F'03) received the Ph.D. degree from Stanford University, Stanford, CA, 1988.

He received the IEEE Sarnoff Award in 2010 and the IEEE Microwave Prize in 1997. He received the Doluca Family Endowed Chair in Electrical and Computer Engineering, University of California, Santa Barbara (UCSB). He directs the UCSB node of the National Science Foundation Nanofabrication Infrastructure Network and the Semiconductor Research Corporation Nonclassical Complementary-Metal-Oxide Research Center.

**Larry A. Coldren** (S'67–M'72–SM'77–F'82) received the Ph.D. degree in electrical engineering from Stanford University, Stanford, CA, in 1972.

He is Fred Kavli Professor of optoelectronics and sensors with the University of California, Santa Barbara (UCSB). After 13 years in the research area at Bell Laboratories, Murray Hill, NJ, he joined UCSB in 1984, where he now holds appointments with the Department of Materials and the Department of Electrical and Computer Engineering. In 1990, he co-founded Optical Concepts, later acquired as Gore Photonics, Newark, DE, to develop novel vertical-cavity surface-emitting laser (VCSEL) technology, and in 1998, he co-founded Agility Communications, later acquired by JDS Uniphase (JDSU) Corporation, Milpitas, CA, to develop widely-tunable integrated transmitters. At Bell Laboratories, he initially worked on waveguided surface-acoustic-wave signal processing devices and coupled-resonator filters. He later developed tunable coupled-cavity lasers using novel reactive-ion etching technology that he created for the new InP-based materials. At UCSB, he continued work on multiple-section tunable lasers in 1988, inventing the widely-tunable multi-element mirror concept, which is now used in some JDSU products. During this period, he also made seminal contributions to efficient designs that continue to be implemented in practical devices to this day. More recently, his group has developed high-performance InP-based photonic integrated circuits as well as high-speed VCSELs and they continue to advance the underlying materials growth and fabrication technologies. He has authored or co-authored more than 1000 journal and conference papers, seven book chapters, and one textbook and has been issued 64 patents.

Prof. Coldren is a fellow of the Optical Society of America and the Institution of Electrical Engineers, and a member of the National Academy of Engineering. He was a recipient of the 2004 John Tyndall and 2009 Aron Kressel Awards. He has presented dozens of invited and plenary talks at major conferences.